Dual-Band Perfect Absorber for Multispectral Plasmon-Enhanced Infrared Spectroscopy

Kai Chen,[†,‡] Ronen Adato,[‡] and Hatice Altug[*]

Department of Electrical and Computer Engineering, Boston University, Boston, Massachusetts 02215, United States. [†]Present address: Experimental Physics 5, University of Wuerzburg, Wuerzburg 97074, Germany. [‡]These authors contributed equally to this work.

ABSTRACT

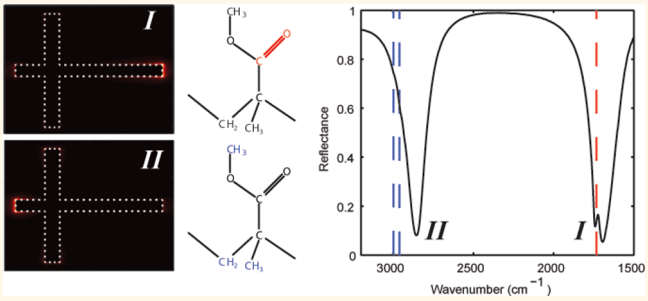

Metamaterial-based perfect absorbers utilize intrinsic loss, with the aid of appropriate structural design, to achieve near unity absorption at a certain wavelength. For most of the reported absorbers, the absorption occurs only at a single wavelength where plasmon resonances are excited in the nanostructures. Here we introduce a dual-band perfect absorber based on a gold nanocross structure. Two bands of maximum absorption of 94% are experimentally accomplished by breaking the symmetry of the cross structure. Furthermore, we demonstrate the two bands can be readily tuned throughout the mid-infrared with their associated resonances giving rise to large near-field enhancements. These features are ideal for multiband surface-enhanced infrared spectroscopy applications. We experimentally demonstrate this application by simultaneously detecting two molecular vibrational modes of a 4 nm thick polymer film utilizing our proposed absorber. Furthermore, in response to variations in the interaction strength between the plasmonic and molecular dipoles, we observe an anticrossing behavior and modification in the spectral line shape of the molecular absorption peak, which are characteristic of the coupling between the two modes.

KEYWORDS: plasmonics · metamaterials · perfect absorber · spectroscopy · SEIRA

Metamaterials (MMs) are artificially constructed materials, which consist of subwavelength elements whose spatially averaged response can be treated as that of a homogeneous medium with a characteristic effective permittivity (ε) and permeability (μ).[1−3] This permits the optical properties, as governed by these constitutive parameters, of the MM to be engineered deliberately, enabling exotic, negative refractive index,[1−3] strongly dispersive,[4] or high permittivity materials[5] not found in nature. Such unusual properties have enabled exciting applications such as perfect lenses[6−8] or electromagnetic invisibility cloaks.[9] Another recent application of MMs is the perfect absorber (PA) concept, in which the resonant MMs can result in near unity absorbance over a small frequency range.[10,11] MM PAs are promising for applications such as sensitive detectors, thermal imaging or emitters, and thin film photovoltaic solar cells.[12]

The PA effect is typically explained in terms of engineered impedance matching.[10] The MM is designed such that it exhibits both electric and magnetic resonances, the strengths of which are tuned such that the bulk effective impedance of the MM, $Z_{eff} = (\mu_{eff}/\varepsilon_{eff})^{1/2}$,[10] is matched to that of the incident medium (typically vacuum/air, such that $Z_{eff} = 1$). This results in a reflection coefficient, $r = 0$, for the MM, and the majority of the incident light is absorbed. Multiple MM layers can thus be stacked to achieve unity absorption. Such structures were first demonstrated at microwave frequencies using a combination of split-ring resonators (SRRs) and cut wire pairs to elicit and tune the electric and magnetic dipolar responses independently.[10] Efforts to demonstrate MM PAs at progressively higher frequencies have converged on a theme of simplified designs that essentially consist of a nanoparticle resonator separated a small distance from a thick metal film by a thin dielectric spacer.[11] While this design sacrifices a measure of independence of the electric and magnetic response, it is more amenable to the lithographic fabrication techniques used at higher frequencies. Recently, it has also been noted that such an absorber design can intuitively (and more appropriately) be treated as a resonator coupled to a single input transmission line.[13] Instead of ε_{eff} and μ_{eff} of the MM,

* Address correspondence to altug@bu.edu.

Received for review June 12, 2012 and accepted July 30, 2012.

Published online August 24, 2012
10.1021/nn3026468

one considers the radiative and intrinsic damping rates, γ_E and γ_0, respectively, of the resonator and varies the spacer layer thickness such that γ_E is reduced until they are equal, which results in critical coupling and unity absorption.[13]

This description is especially advantageous for evaluating recently proposed MM PAs used in biosensing applications where resonance shifts are monitored in a manner similar to typical refractive index sensors.[14] In fact, it leads one to immediately note that, for operation in the near-IR and longer wavelengths, MM PAs should be characterized by high *Q* resonances as they operate in a regime of reduced radiation damping. This feature is also very attractive for surface-enhanced spectroscopy applications, especially surface-enhanced infrared absorption (SEIRA), which leverages mid-IR plasmonic resonances.[15−20] Indeed, several recent studies have shown narrow line width modes with reduced damping in nanoparticle lattices[16,21] and complex MMs[22] lead to higher field enhancements and therefore increased spectroscopic signals, indicating that MM PAs are promising candidates for SEIRA spectroscopy.

In many applications, and especially for SEIRA, a significant drawback of MM PAs is their narrowband response, resulting from the fact that their behavior relies on the resonances of small metallic particles. PA structures with dual or multiple bands are desirable for a number of promising applications such as selective optical filters, multiplexing detector arrays, as well as the aforementioned biochemical sensing applications. Particularly, in the field of mid-IR spectroscopy, it is of great interest to simultaneously monitor multiple spectral fingerprint regions characteristic of different chemical or biological moieties.[23] The ability to monitor multiple absorption bands allows one to correlate and study structural changes between different molecular regions[24] and is critical to the accurate identification of molecular species and can even enable the detection and characterization of complex biological entities, such as cells[25−29] or bacteria.[30]

Recent efforts to achieve dual- or multiband PAs[31,32] are, however, limited in their applicability to IR spectroscopy. For example, while a recent design[32] obtained resonances with >90% absorbance at 3.3 and 3.9 μm, this range is dwarfed by the mid-IR spectral range which extends from ~3 to 20 μm (3000−500 cm^{-1}). Furthermore, for SEIRA applications, it is essential to be able to readily tune the frequency of a given resonance to that of the vibrational mode of interest in order to maximize its enhancement.[17,19,22,33]

To this end, we demonstrate here the use of an asymmetric cross-shaped nanoparticle antenna separated by a thin MgF_2 layer on a thick gold film as a compact, single-element, dual-band PA. The design is based on our previous work[33] which noted that a thin bar can be used as a wire reflector in the mid-IR and implemented in a T-shaped nanoparticle to set up compact quarter-wave monopole resonances. The asymmetric cross-shaped structure acts to combine two such elements, with different antenna arm lengths, thereby providing two broadly tunable resonances dependent on the symmetry of the structure. A critical departure we observe in the MM PA implementation is that as the resonances are tuned they maintain very similar amplitudes and line widths. In the previous study, which measured extinction from a nanoparticle scatterer, the tunable range of the structure was potentially limited in practice by the fact that the short wavelength resonance was significantly decreased in amplitude owing to its smaller induced dipole moment.[33] In contrast, here we demonstrate experimentally 94% absorption for both bands even when they are separated by ~3 μm (1300 cm^{-1}). Furthermore, we demonstrate that both resonant modes support large field enhancements and can be extensively tuned throughout the majority of the mid-IR. These unique characteristics make the MM PA ideal for multiband SEIRA spectroscopy, which we demonstrate here by simultaneously enhancing multiple molecular resonances, separated by ~3 μm (1200 cm^{-1}), of a thin polymer film (4 nm thick). Finally, by varying the strength of the interaction between the plasmonic and molecular resonances, we observe the characteristic anticrossing behavior indicative of the coupling between the two modes.[34−37]

RESULTS AND DISCUSSION

The concept and features of the proposed dual-band PA are presented in Figure 1. A typical PA unit cell, illustrated in panel a, consists of a nanoparticle placed on top of a thick metal film, separated by a spacer layer. In the current work, we have used gold (Au) for both the particle and the film, and magnesium fluoride (MgF_2) for the spacer layer. The structures are all fabricated on a silicon substrate. Incident radiation polarizes the nanoparticle antenna. Due to the antenna's close proximity to the metal film, near-field coupling between the two generates antiparallel currents at the antenna and the metal film surface. The induced polarization and current loop drive electric and magnetic dipole responses of the PA, respectively, providing a means with which to tune its effective ε and μ and thus its optical properties.[10,11,13] Manipulating the effective optical constants allows the PA to impedance match to free space, thereby minimizing reflection. This effect, in conjunction with the blocking of transmission by the thick Au film, leads to near total, or "perfect", absorption.

The generic nature of this effect enables a wide variety of particle geometries to be used to achieve the required resonant electric/magnetic response. These range from split-ring resonators[10] to metallic strips,[13] patches, or discs.[14] The majority of these designs rely on a single, half-wave dipolar response where the plasmonic resonator supports a full period current oscillation. Instead, the asymmetric unit cell

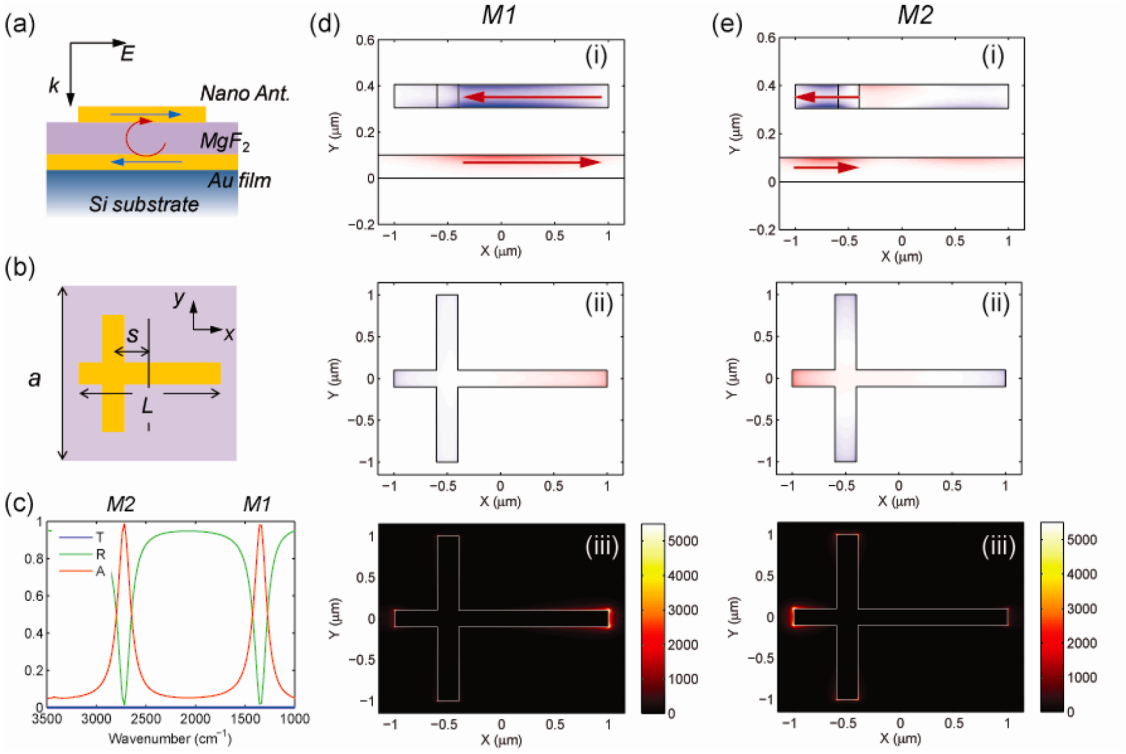

Figure 1. Geometry and operation principles of the dual-band perfect absorber. (a) General schematic of a perfect absorber. (b) Asymmetric unit cell used here and (c) characteristic dual-band response. The incident electromagnetic field is polarized in the *x* direction, *a* is the unit cell size (square lattice). The two antenna modes associated with the long and short wavelength resonances (M_1 and M_2) are characterized in (d) and (e), respectively. The conduction current (i), charge density (ii), and near-field intensity enhancement ($|E/E_0|^2$) (iii) are shown. The current density is shown in the $x-z$ plane, illustrating the antiparallel currents that set up the magnetic dipole response, while the charge density in the $x-y$ plane at the top surface of the particle illustrates the electric dipole response.

shown in Figure 1b can be used to obtain a dual-band absorber. For light polarized in the *x*-direction, the perpendicular (*y*-oriented) bar acts as a wire reflector, presenting an effective mirror plane.[33,38] When the *y*-oriented bar is placed at a noncentral position, the structure is divided into two nondegenerate $\lambda/4$ monopole antennas, whose lengths are increased or decreased by the asymmetry parameter, *S*, as defined in Figure 1b. Each *x*-oriented arm supports resonant modes associated with a *half-period* of the sinusoidal current mode confined to its physical length.[38] The two first-order resonant modes, M_1 and M_2, are approximately related to two antenna arm lengths, L_1 and L_2 *via*

$$\lambda_{1(2)} = (2n_{\text{eff}}/m)(2L_{1(2)}) + C \qquad (1)$$

where *m*, the mode number, is equal to 1 for the first-order modes and the effective lengths are given by $L_1 \sim L/2 + S$ and $L_2 \sim L/2 - S$. This effect is demonstrated in the FDTD simulations in Figure 1c–e. The calculations are done for a cross antenna PA with $L = 2.0\,\mu$m, $P_X = P_Y = 2.3\,\mu$m, $S = 500$ nm, and a MgF_2 film thickness of 205 nm. Panels d-i and e-i show the calculated conduction current densities taken through a cross sectional cut in the $x-z$ plane at $y = 0$. For the long wavelength mode (M_1), the current flow is confined almost entirely to the longer (L_1) arm and the region of the Au film directly beneath it. Similarly, the short wavelength (M_2) mode is primarily associated with the shorter (L_2) antenna arm. Thus, while this dual monopole behavior was originally observed in nanoparticle scattering implementations, we observe the structure to behave similarly when the particle is placed in close vicinity to the Au film to form the resonant element of a PA. In particular, the image charges result in antiparallel currents localized directly beneath the excited antenna arm (*i.e.*, L_1 for M_1, L_2 for M_2). This forms the current loops (highlighted by the red arrows in the figure, which point in the direction of current flow) which generate the magnetic dipole response of the structure. The electric dipolar response of the nanoantenna also follows similarly, as illustrated by the charge density at the top surface of the particle (panels d-ii and e-ii) and the near-field (intensity) enhancement associated with strong charge buildup at opposite ends of the two antenna arms (panels d-iii and e-iii). The resultant transmission (*T*), reflection (*R*), and absorption ($A = 1 - R - T$) spectra are shown in Figure 1c. The reflection and absorption display clear resonances at the two mode frequencies, while the transmission is essentially zero throughout, being blocked by the semi-infinite Au film (see Supporting Information).

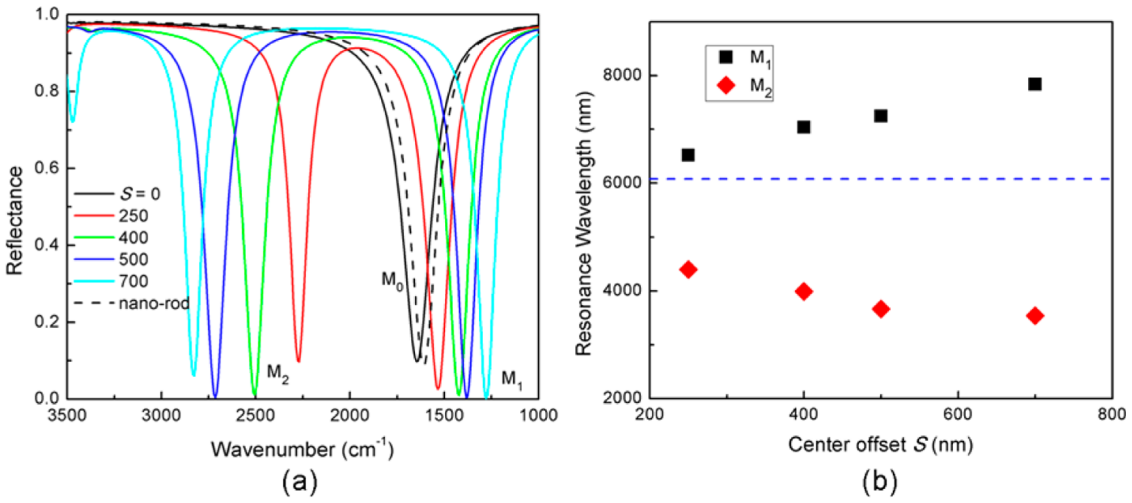

Figure 2. Numerical simulation of the reflectance of the absorber. (a) Reflectance spectra of the absorber as *S* increases. The MgF_2 layer is 205 nm thick. When the cross is symmetric (*S* = 0), only one absorption dip (M_0) is observed. The spectra of a single nanorod polarized along the *x*-axis (black dashed line) is also shown for comparison. (b) Relationship between the center offset *S* and the two resonance mode wavelengths. Resonance mode M_1 linearly red shifts, while M_2 blue shifts as *S* increases. The blue dashed line indicates the resonance wavelength of mode M_0.

An important aspect of the dual-band PA observed here is the high degree of symmetry in the characteristics of the two resonant modes despite being separated by >1000 cm^{-1}. Both modes exhibit similar peak absorbance on resonance (98.1 and 98.7% for M_1 and M_2, respectively) and similar line widths (fwhm = 167.5 cm^{-1} for both). This is in contrast to the nanoparticle implementation originally conceived in ref 33, where a detuning of ~3.5 μm resulted in very different reflectance amplitudes of the two modes, as well as very disparate line widths. Similarly, simulations of the nanoparticle analogue to the PA investigated in Figure 1 (*i.e.*, the same structure, but on a semi-infinite MgF_2 substrate, without the Au film or Si substrate beneath) result in the same two modes, M_1 and M_2, but with reflectance amplitudes of 0.8 and 0.5 (see Supporting Information) on resonance. Most importantly, the degree of symmetry between the two modes carries over to the near-field response of the PA. On average, a near-field intensity enhancement[39] of ~2500 is observed at the tip ends of the antenna arms associated with M_1 and M_2 at each resonance for the structure in Figure 1 (*S* = 500 nm). In contrast, much lower and highly asymmetric enhancement factors of ~400 and 1300 are observed for M_1 and M_2 in the nanoparticle analogue (see Supporting Information).

The fact that the two resonances in the PA display large and roughly equal field enhancement is highly advantageous for SEIRA measurements. The possibility of dramatically enhancing near-fields over two widely separated spectral windows would enable one to monitor the interactions between different molecules or conformational changes associated with different structural groups in, for example, proteins. In order to do so, it is necessary to be able to easily position the resonances throughout the mid-IR. This capability is demonstrated in Figure 2,

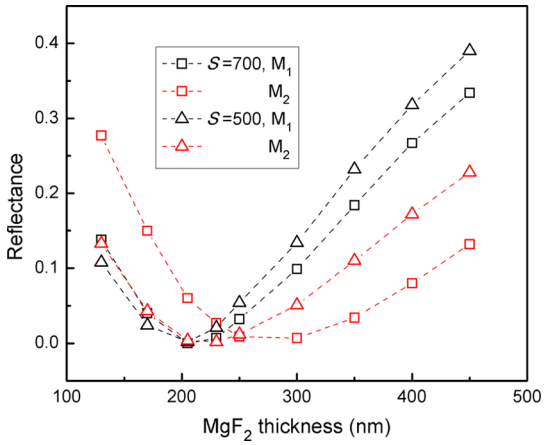

Figure 3. Relationship between the reflectance of the two resonance modes (black for M_1 and red for M_2) and the thickness of the MgF_2 layer for *S* = 700 nm (triangle) and *S* = 500 nm (square). These two modes, M_1 and M_2, reach minimum of reflectance at different MgF_2 thickness due to the different coupling strength of the two modes. The dashed lines serve as a guide for the eye.

which shows the reflectance spectra for several different PA structures with differing values of *S*. As *S* is increased, the two antenna arm lengths, L_1 and L_2, increase and decrease, respectively, red and blue shifting the associated mode, as shown in Figure 2b. In qualitative agreement with eq 1, the resonant wavelength of M_1 increases linearly with *S*. The initial linear decrease in the resonant wavelength of M_2 that saturates is similar to the observations in our previous work and can be explained *via* circuit theory.[33] The additional feature observed at higher frequencies in the graph for *S* = 700 nm is associated with the *m* = 3 mode of the longer monopole, as expected from eq 1. Significantly, the two resonances exhibit similar fwhm values and reflectance minima below 10% throughout the tuning range.

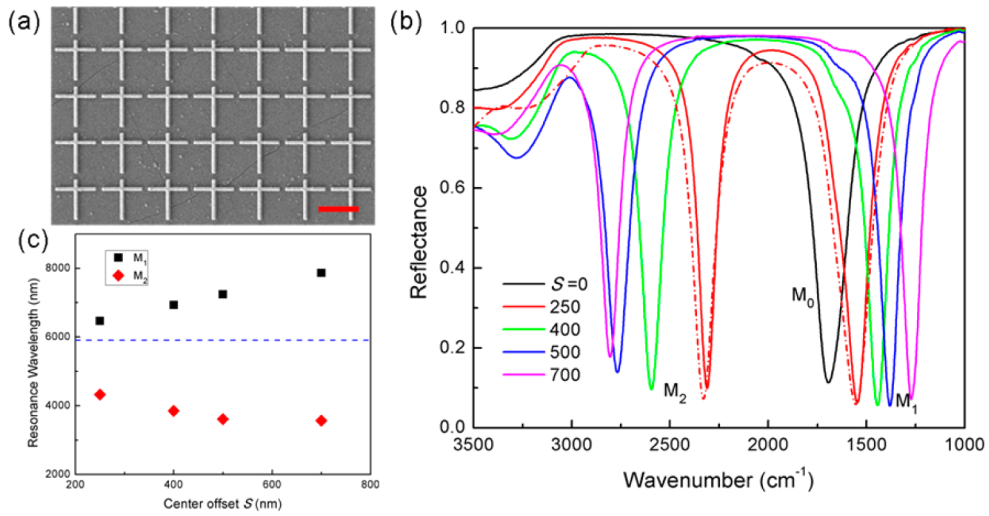

Figure 4. Experimental data of the fabricated absorber. (a) Typical SEM image of the fabricated dual-band perfect absorber. The scale bar is 2 μm in length. (b) Experimentally measured reflectance spectra of the absorber at difference values of S when the MgF_2 is 235 nm thick (solid curves). The dashed red curve corresponds to a sample with a 300 nm thick MgF_2 layer, yielding ~94% absorbance at both M_1 and M_2. (c) Relationship of the resonance wavelengths of the two modes with the center offset S for 235 nm thick MgF_2 spacer. The blue dashed line gives the resonance wavelength of mode M_0 for reference.

The critical importance of the spacer thickness, h, which controls radiation damping, is demonstrated in Figure 3. In the figure, the reflectance values at the minima for the two modes of the S = 500 and 700 nm structures are plotted for a range of different MgF_2 thicknesses. In all cases, the reflectance is minimized for a specific thickness of the spacer layer, corresponding to the value of h at which $\gamma_E = \gamma_0$.[13] For the S = 500 nm structure, these thicknesses fall in close vicinity to each other for both M_1 and M_2, and as a result, nearly 100% absorption (0% reflectance) is achieved for a MgF_2 thickness of ~205 nm. In contrast, for the S = 700 nm structure, the thickness at which M_2's reflectance is minimized is ~100 nm larger than the optimal one for M_1. Despite this fact, the variation is slow enough (as a function of h) for both modes such that a ~98% absorption can be achieved for both modes when h is ~240 nm. In fact, the graph illustrates a great deal of stability in the reflectance minima, to the extent that the MgF_2 thickness can be varied by as much as 200 nm while maintaining R < 10%. This high degree of control over the damping properties of the resonant modes allows the PA geometry to be extremely effective in leveraging the multiple resonances of our composite nanoantenna for dual-band absorption. The dual-band PA design implemented here can thus support high Q resonances with strong near-field enhancement over two broadly tunable modes, making it extremely promising as a SEIRA substrate capable of enhancing multiple molecular absorption bands simultaneously.

To test this experimentally, we fabricated PA samples similar to those in the FDTD simulations. The film layers of the samples were prepared by first evaporating 100 nm Au followed by MgF_2 (various thicknesses) for the spacer layer, all on a Si substrate. The nanoparticle resonators were fabricated on top of the MgF_2 *via* e-beam lithography (EBL) and a lift-off process. Figure 4 presents the experimentally achieved properties of the fabricated PA samples. A typical sample is shown in the scanning electron microscope (SEM) image in Figure 4a. The particle dimensions are similar to those in the FDTD simulations, with $L \sim 2\ \mu$m, $w \sim 0.17\ \mu$m, and $a = 2.3\ \mu$m. The reflectance spectra, measured with an FTIR and IR microscope (Bruker; see Methods) are shown in Figure 4b and are in close agreement with numerical simulations. The appearance of the two modes, M_1 and M_2, and their tuning in opposite directions with increasing S, is also in agreement with Figure 2. A slight reduction in the minimal reflectance is observed in comparison with the FDTD results, with M_1 ranging from ~93 to 95% and M_2 from 82 to 91%. This is potentially a result of our measurement setup as well the MgF_2 film quality (see Methods). In general, the experimental data illustrate the high quality of the structures and their resonances and thus suitability for SEIRA measurements.

As a proof-of-concept experiment, we demonstrate the simultaneous detection of two molecular specific vibration modes of a thin PMMA film on top of the multiresonant PA. PMMA polymer is used as a model system because it has several well-characterized absorption bands in the infrared range. Here, we targeted the C−H and C═O absorption bands, which are separated by ~1200 cm^{-1}. The PMMA film was ~4 nm thick based on spectroscopic ellipsometry measurements (JA Woolham). The reflection spectra of the PMMA-coated PA are shown in Figure 5. The absorption features of PMMA are observed on the reflectance spectra of the two resonant modes. The strong dip around 1740 cm^{-1} range is due to the C═O band stretch, and the two small dips at 2955 and 2995 cm^{-1}

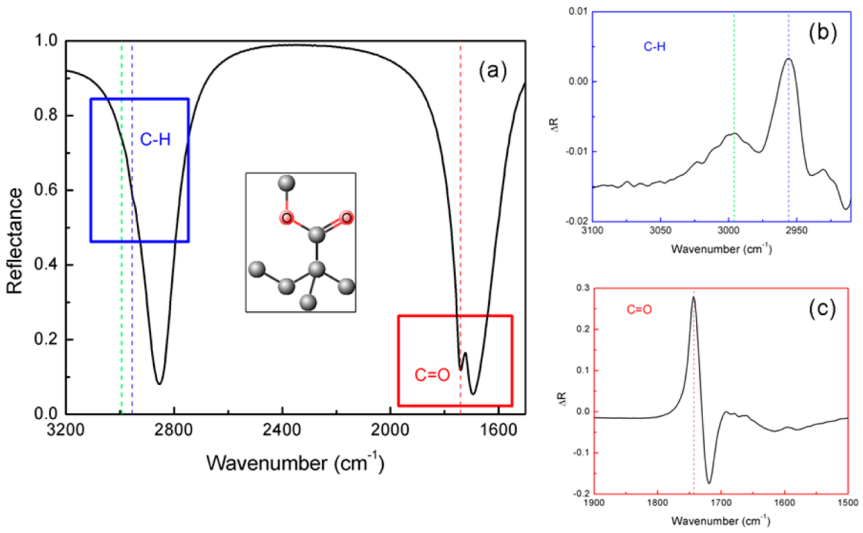

Figure 5. SEIRA spectroscopy of PMMA on the absorber. (a) Reflectance spectrum of the absorber after the coating of a 4 nm thick PMMA film. Characteristic vibrational stretches of C═O and C−H are visible on the spectrum as indicated by the dashed lines. The inset shows the repeat unit of PMMA polymer. (b) Reflectance difference spectrum of the C−H group and (c) C═O band.

range are corresponding to vibrational stretches of the C−H group. The spectral positions of these vibrational bands, especially C═O band, are slightly off from their general values. We will elaborate on this effect later in the paper. For a better display of the absorbance of the molecular signatures, a reflectance difference spectrum, as shown in Figure 5b,c, was calculated by taking the reflectance difference on the same sample before and after PMMA coating. Additionally, because the PMMA refractive index contains a nondispersive, $n_\infty \approx 1.5$, component, aside from any effect related to coupling to the PMMA absorption bands, coating the PA sample with the polymer film induces a red shift in the resonance frequencies due to the effective increase in the background dielectric constant (ref 22 and Supporting Information). In order to account for this effect, we used a frequency-shifted version of the bare PA spectra in our subtraction (see Methods). The characteristic absorption bands are thereby explicitly revealed in the difference spectrum. As expected, the intensity of the C═O stretch is the largest because of its intrinsic large dipole moment and the good spectral overlap with the resonance modes. The simultaneous detection of the two PMMA molecular vibrational stretches, especially the C−H stretches with small dipole moments, exclusively demonstrates that our proposed perfect absorber structure is well suitable for molecular vibrational spectroscopy and furthermore for simultaneous detections of multiple chemical or biological agents. To the best of our knowledge, this is the first time that a perfect absorber is applied for multiband infrared spectroscopy.

In addition, it is interesting to notice that the C═O stretch is distorted from its normal Lorentzian shape exhibiting an asymmetric Fano profile-like shape, as can be seen in Figure 5c. This is attributed to the strong interaction between the molecular dipole and the plasmon modes of the perfect absorber resonances. Coupling between the plasmonic and the PMMA vibrational modes results in the line shape modifications and spectral shifts in the absorption minima.[17,34−36] This effect is clearly demonstrated in Figure 6a, where the C═O absorption dips of PMMA are apparently shifted from their usual spectral position at 1733 cm^{-1}, as indicated by the red dashed line in the graph. The value of 1733 cm^{-1} was determined by the absorption spectrum of a thin PMMA film on a bare Si substrate using the FTIR microscope. As shown in the graph, the spectral shift of the PMMA absorption dip is strongly dependent on the spectral position of the plasmon resonance mode: when the plasmon resonances are larger than 1733 cm^{-1}, the absorption dips red shift (in terms of wavelength); on the other hand, when the plasmon modes are smaller than 1733 cm^{-1}, the dips blue shift. When the PA and vibrational resonance frequencies are closely aligned, a clear splitting is observed (red curve in Figure 6a). To further study this plasmon−molecule interaction, we fabricated a series of samples with resonances across the 1733 cm^{-1} range. Reflectance spectra were acquired before and after coating the samples with PMMA. The frequencies of the two minima that result from the interaction between the PA resonance and the vibrational mode were plotted against the frequency of the initial, bare PA resonance (denoted $\omega_{PA(0)}$) for each sample. The resultant data points are shown in Figure 6b,c as the triangular markers. The horizontal red dashed line gives the frequency of the PMMA C═O band at 1733 cm^{-1}. The blue dotted line is a slope = 1 line, corresponding to the bare PA's initial resonance frequency (*i.e.*, a plot of $\omega_{PA(0)} = \omega_{PA(0)}$). The dashed blue line has a shifted slope to account for the red shifting of

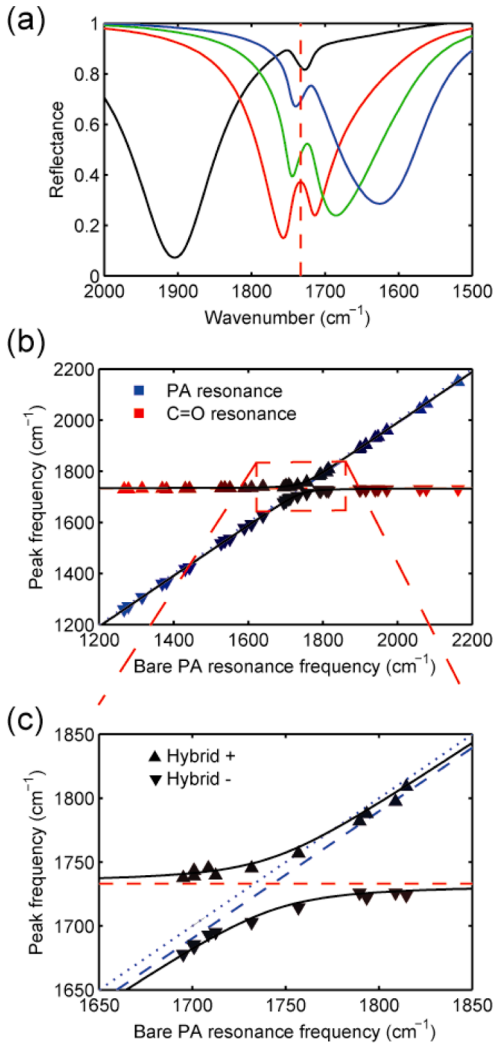

Figure 6. Coupling between plasmonic and vibrational modes. (a) Reflectance spectra of a PA sample coated with the PMMA film as M_1 is tuned through the C═O band at 1733 cm^{-1} (red dashed vertical line). Tuning is accomplished by varying the center offset, *S*, from 0, 250, 400, to 500 nm (black, red, green, and blue curves, respectively). (b) Local minima positions (*i.e.*, absorption peaks) taken from a range of samples, plotted against the bare PA samples' resonance frequencies. The degree of blue/red coloring indicates the resemblance to the bare PA or C═O vibrational mode, respectively. (c) Expanded view of the graph in (b), focusing on the region where the resonances are hybridized. The horizontal red dashed line gives the frequency of isolated C═O PMMA absorption line, while the dotted and dashed blue lines correspond to $E_{PA(0)}$ and $E_{PA(1)}$ as described in the text. The solid black lines are calculated from eq 2 with a coupling energy of 2.5 meV.

the PA resonance due to the nondispersive component of the PMMA refractive index, corresponding to the $\omega_{PA(1)} = [1 + \Delta\omega/\omega_{PA(0)}]\omega_{PA(0)}$ (see also Supporting Information). When the plasmonic resonance is detuned from the C═O band, the absorption minima lie at their respective original (noninteracting) positions along the dashed lines. Tuning the resonance frequency of the plasmon mode toward that of the C═O band at 1733 cm^{-1} greatly increases the strength of the interaction between the two modes, and we observe a characteristic mode splitting and anticrossing (see Figure 6c). Similar effects have been observed in association with plasmon−exciton coupling in *J*-aggregate-coated systems at visible frequencies,[34,37] as well as simple pedagogical coupled oscillators.[36] In particular, the interaction Hamiltonian of the system can be diagonalized (see ref 34 and Supporting Information) to yield the eigenvalues

$$E_{\pm} = \frac{E_{PA(1)} + E_{C=O}}{2} \pm \sqrt{\frac{(E_{PA(1)} - E_{C=O})^2}{4} + V_{12}^2} \quad (2)$$

corresponding to the hybrid + and − states ($E_{\pm}$). The energies of the hybrid states depend on the energies of the uncoupled states, $E_{PA(1)} = \hbar\omega_{PA(1)}$ and $E_{C=O}$, and the coupling strength, V_{12}. This results in the characteristic anticrossing behavior observed here. The peak in reflection which corresponds to a reduction in absorption between the two peaks (see red curve in Figure 6a) results from the coherent interference between the two hybrid modes and is closely related to electromagnetic induced transparency (EIT) and Fano interference. Importantly, because essentially absorption is measured here, the interference effects are a direct result of the coupling between the two resonances as opposed to far-field measurements in which EIT and Fano-like effects can occur even in the absence of direct energy exchange between two resonant modes.[40]

On the basis of the data, the size of the splitting can be used to estimate the coupling strength of the interaction *via*[34]

$$V_{12} = \frac{1}{2}\sqrt{(E_+ - E_-)^2 - (E_{PA(1)} - E_{C=O})^2} \quad (3)$$

Inserting the values from the data when the PA and vibrational resonance frequencies are aligned (*i.e.*, red curve in Figure 6a) into eq 3, we estimated the coupling strength to be 2.1−2.5 meV depending on whether the approximation $E_{PA(1)} \approx E_{PA(0)}$ or the value for $E_{PA(1)}$ computed from the dashed blue line's fit is used in the formula. Using V_{12} = 2.5 meV (20.1 cm^{-1}) in eq 2 allows one to compare the trends in the frequencies of the analytical eigenvalues (black lines in Figure 6b,c) with the peak positions observed in the data. The close agreement is evident in Figure 6c. While the coupling energy value is smaller than observed in the studies of *J*-aggregates,[37] it is a comparable fraction of the line widths of the two resonances.[41] Considering the fact that the intrinsic oscillator strengths associated with vibrational transitions are typically orders of magnitude weaker than those of electronic transitions, these results point out the significant ability of the high *Q* PA resonance in enhancing the light−matter interaction.

CONCLUSION

In conclusion, we have demonstrated a highly tunable dual-band MM PA based on a multiband

composite nanoparticle antenna. Significantly, in contrast to the earlier particle implementation of the structure, its use as the resonant element of a PA allows for both its resonances to maintain large amplitudes and relatively high *Q* factors as they are tuned throughout the mid-IR. This feature makes the implementation of PAs in biosensing applications extremely promising, especially SEIRA, given the importance of monitoring multiple spectral windows in mid-IR spectroscopy. To demonstrate this, we utilized our two tunable resonances to simultaneously detect widely separated multiple molecular vibrational modes using thin PMMA film as a model analyte. Three molecular modes of C═O and C−H in a 4 nm thick PMMA film were revealed by matching our plasmonic resonances with the vibrational modes. We also observed strong interaction between the plasmonic resonances and molecular dipoles manifested by the modification of the absorption line shape and spectral position of the vibrational stretches of C═O moiety. These results demonstrate the potential for multiband SEIRA, which can enable the tracking of several characteristic molecular vibrational modes, making it possible to identify different molecular species or even larger complex biological entities simultaneously.

METHODS

PA Sample Fabrication. In brief, the gold film and MgF_2 spacer layer were deposited onto a Si substrate using electron-beam evaporation consecutively. The gold cross nanoantennas were fabricated *via* standard electron beam lithography and lift-off. A layer of PMMA (950-A5, Michrochem) was spin-coated on top of the MgF_2 layer. EBL was carried out in a Zeiss 40 VP system followed by development of the samples. Then, a layer of gold (100 nm) was deposited by e-beam evaporation without any adhesion layer. Finally, lift-off was performed by immersion in acetone. Figure 5a represents a typical SEM image of the fabricated sample with $S = 400$ nm.

FTIR Measurements. The reflection spectra of the samples were recorded using a Fourier transform infrared (FTIR) spectrometer and IR microscope (Bruker IFS 66/s and Hyperion 1000). Reflectance was collected with a 0.4 NA Schwarzchild objective and recorded by a liquid-nitrogen-cooled mercury cadmium telluride (MCT) detector.

The difference spectra displayed in Figure 5b,c correspond to the calculation, $\Delta R = R_0' - R_A$, where R_0' and R_A are the frequency-shifted bare PA and PMMA-coated PA reflectance spectra, respectively. The frequency shift is accomplished by transforming the original bare PA data, $R_0(\tilde{\nu})$, according to the transformation, $R'_0 = R_0(\tilde{\nu}) \rightarrow R_0(\tilde{\nu} - \Delta\tilde{\nu})$, performed *via* the built-in frequency calibration function in OPUS software (Bruker Optics, ver. 5.5).

Conflict of Interest: The authors declare no competing financial interest.

Acknowledgment. This work is supported in part NSF CAREER Award (ECCS-0954790), ONR Young Investigator Award, Massachusetts Life Science Center New Investigator Award, NSF Engineering Research Center on Smart Lighting (EEC-0812056), Boston University Photonics Center, and Army Research Laboratory.

Supporting Information Available: Log-scale plot of Figure 1c. Additional FDTD simulations. Additional discussion related to the plasmon−vibrational mode coupling. This material is available free of charge *via* the Internet at http://pubs.acs.org.

REFERENCES AND NOTES

1. Smith, D. R.; Padilla, W. J.; Vier, D.; Nemat-Nasser, S.; Schultz, S. Composite Medium with Simultaneously Negative Permeability and Permittivity. *Phys. Rev. Lett.* **2000**, *84*, 4184–4187.
2. Smith, D. R.; Pendry, J. B.; Wiltshire, M. C. K. Metamaterials and Negative Refractive Index. *Science* **2004**, *305*, 788–792.
3. Shalaev, V. M. Optical Negative-Index Metamaterials. *Nat. Photonics* **2007**, *1*, 41–48.
4. Zhang, S.; Genov, D. A.; Wang, Y.; Liu, M.; Zhang, X. Plasmon-Induced Transparency in Metamaterials. *Phys. Rev. Lett.* **2008**, *101*, 047401.
5. Choi, M.; Lee, S. H.; Kim, Y.; Kang, S. B.; Shin, J.; Kwak, M. H.; Kang, K.-Y.; Lee, Y.-H.; Park, N.; Min, B. A Terahertz Metamaterial with Unnaturally High Refractive Index. *Nature* **2011**, *470*, 369–373.
6. Pendry, J. Negative Refraction Makes a Perfect Lens. *Phys. Rev. Lett.* **2000**, *85*, 3966–3969.
7. Fang, N.; Lee, H.; Sun, C.; Zhang, X. Sub-Diffraction-Limited Optical Imaging with a Silver Superlens. *Science* **2005**, *308*, 534–537.
8. Taubner, T.; Korobkin, D.; Urzhumov, Y.; Shvets, G.; Hillenbrand, R. Near-Field Microscopy through a SiC Superlens. *Science* **2006**, *313*, 1595.
9. Schurig, D.; Mock, J. J.; Justice, B. J.; Cummer, S. A.; Pendry, J. B.; Starr, A. F.; Smith, D. R. Metamaterial Electromagnetic Cloak at Microwave Frequencies. *Science* **2006**, *314*, 977–980.
10. Landy, N. I.; Sajuyigbe, S.; Mock, J. J.; Smith, D. R.; Padilla, W. J. Perfect Metamaterial Absorber. *Phys. Rev. Lett.* **2008**, *100*, 207402.
11. Liu, X.; Starr, T.; Starr, A. F.; Padilla, W. J. Infrared Spatial and Frequency Selective Metamaterial with Near-Unity Absorbance. *Phys. Rev. Lett.* **2010**, *104*, 207403.
12. Aydin, K.; Ferry, V. E.; Briggs, R. M.; Atwater, H. A. Broadband Polarization-Independent Resonant Light Absorption Using Ultrathin Plasmonic Super Absorbers. *Nat. Commun.* **2011**, *2*, 517.
13. Wu, C.; Nuener, B., III; Shvets, G.; John, J.; Milder, A.; Zollars, B.; Savoy, S. Large-Area Wide-Angle Spectrally Selective Plasmonic Absorber. *Phys. Rev. B* **2011**, *84*, 75102.
14. Liu, N.; Mesch, M.; Weiss, T.; Hentschel, M.; Giessen, H. Infrared Perfect Absorber and Its Application as Plasmonic Sensor. *Nano Lett.* **2010**, *10*, 2342–2348.
15. Kundu, J.; Le, F.; Nordlander, P.; Halas, N. J. Surface Enhanced Infrared Absorption (SEIRA) Spectroscopy on Nanoshell Aggregate Substrates. *Chem. Phys. Lett.* **2008**, *452*, 115–119.
16. Adato, R.; Yanik, A. A.; Amsden, J. J.; Kaplan, D. L.; Omenetto, F. G.; Hong, M. K.; Erramilli, S.; Altug, H. Ultra-Sensitive Vibrational Spectroscopy of Protein Monolayers with Plasmonic Nanoantenna Arrays. *Proc. Natl. Acad. Sci. U.S.A.* **2009**, *106*, 19227–19232.
17. Neubrech, F.; Pucci, A.; Cornelius, T. W.; Karim, S.; Garcia-Extarri, A.; Aizpurua, J. Resonant Plasmonic and Vibrational Coupling in a Tailored Nanoantenna for Infrared Detection. *Phys. Rev. Lett.* **2008**, *101*, 157403.
18. Osawa, M.; Ataka, K.; Yoshi, K.; Nishikawa, Y. Surface-Enhanced Infrared Spectroscopy: The Origin of the Absorption Enhancement and Band Selection Rule in the Infrared Spectra of Molecules Adsorbed on Fine Metal Particles. *Appl. Spectrosc.* **1993**, *47*, 1497–1502.
19. Cubukcu, E.; Zhang, S.; Park, Y.-S.; Bartal, G.; Zhang, X. Split Ring Resonator Sensors for Infrared Detection of Single Molecular Monolayers. *Appl. Phys. Lett.* **2009**, *95*, 43113.
20. Ataka, K.; Kottke, T.; Heberle, J. Thinner, Smaller, Faster: IR Techniques To Probe the Functionality of Biological and

Biomimetric Systems. *Angew. Chem., Int. Ed.* **2010**, *49*, 5416–5424.
21. Adato, R.; Yanik, A. A.; Wu, C.; Shvets, G.; Altug, H. Radiative Engineering of Plasmon Lifetimes in Embedded Nanoantenna Arrays. *Opt. Express* **2010**, *18*, 4526–4537.
22. Wu, C.; Khanikaev, A. B.; Adato, R.; Arju, N.; Yanik, A. A.; Altug, H.; Shvets, G. Fano-Resonant Asymmetric Metamaterials for Ultrasensitive Spectroscopy and Identification of Molecular Monolayers. *Nat. Mater.* **2011**, *11*, 69–75.
23. Ataka, K.; Heberle, J. Biochemical Applications of Surface-Enhanced Infrared Absorption Spectroscopy. *Anal. Bioanal. Chem.* **2007**, *388*, 47–54.
24. Jiang, X.; Zaitseva, E.; Schmidt, M.; Siebert, F.; Engelhard, M.; Schlesinger, R.; Ataka, K.; Vogel, R.; Heberle, J. Resolving Voltage-Dependent Structural Changes of a Membrane Photoreceptor by Surface-Enhanced IR Difference Spectroscopy. *Proc. Natl. Acad. Sci. U.S.A.* **2008**, *105*, 12113–12117.
25. Matthaus, C.; Bird, B.; Miljkovic, M.; Chernenko, T.; Romeo, M.; Diem, M. Infrared and Raman Microscopy in Cell Biology. *Methods Cell Biol.* **2008**, *89*, 275–308.
26. van den Driesche, S.; Witarski, W.; Pastorekova, S.; Breiteneder, H.; Hafner, C.; Vellekoop, M. J. A Label-Free Indicator for Tumor Cells Based on the CH2-Stretch Ratio. *Analyst* **2011**, *136*, 2397–2402.
27. Diem, M.; Boydston-White, S.; Chirboga, L.; Hospital, B. Infrared Spectroscopy of Cells and Tissues: Shining Light onto a Novel Subject. *Appl. Spectrosc.* **1999**, *53*, 148–161.
28. Nasse, M. J.; Walsh, M. J.; Mattson, E. C.; Reininger, R.; Kajdacsy-Balla, A.; Macias, V.; Bhargava, R.; Hirschmugl, C. J. High-Resolution Fourier-Transform Infrared Chemical Imaging with Multiple Synchrotron Beams. *Nat. Methods* **2011**, *8*, 413–416.
29. Fernandez, D. C.; Bhargava, R.; Hewitt, S. M.; Levin, I. W. Infrared Spectroscopic Imaging for Histopathologic Recognition. *Nat. Biotechnol.* **2005**, *23*, 469–74.
30. Naumann, D.; Helm, D.; Labischinski, H. Microbiological Characterizations by FT-IR Spectroscopy. *Nature* **1991**, *351*, 81–82.
31. Bingham, C. M.; Tao, H.; Liu, X.; Averitt, R. D.; Zhang, X.; Padilla, W. J. Planar Wallpaper Group Metamaterials for Novel Terahertz Applications. *Opt. Express* **2008**, *16*, 18565–18575.
32. Jiang, Z. H.; Yun, S.; Toor, F.; Werner, D. H.; Mayer, T. S. Conformal Dual-Band Near-Perfectly Absorbing Mid-Infrared Metamaterial Coating. *ACS Nano* **2011**, *5*, 4641–4647.
33. Adato, R.; Yanik, A. A.; Altug, H. On Chip Plasmonic Monopole Nano-Antennas and Circuits. *Nano Lett.* **2011**, *11*, 5219–5226.
34. Wurtz, G. A.; Evans, P. R.; Hendren, W.; Atkinson, R.; Dickson, W.; Pollard, R. J.; Zayats, A. V.; Harrison, W.; Bower, C. Molecular Plasmonics with Tunable Exciton-Plasmon Coupling Strength in J-Aggregate Hybridized Au Nanorod Assemblies. *Nano Lett.* **2007**, *7*, 1297–1303.
35. Mason, J. A.; Allen, G.; Podolskiy, V. A.; Wasserman, D. Strong Coupling of Molecular and Mid-Infrared Perfect Absorber Resonances. *IEEE Photonics Technol. Lett.* **2012**, *24*, 31–33.
36. Novotny, L. Strong Coupling, Energy Splitting and Level Crossings: A Classical Perspective. *Am. J. Phys.* **2010**, *78*, 1199–1202.
37. Fofang, N. T.; Park, T.-H.; Neumann, O.; Mirin, N. A.; Nordlander, P.; Halas, N. J. Plexcitonic Nanoparticles: Plasmon-Exciton Coupling in Nanoshell-J-Aggregate Complexes. *Nano Lett.* **2008**, *8*, 3481–3487.
38. Balanis, C. A. *Antenna Theory*, 3rd ed.; John Wiley & Sons: Hoboken, NJ, 2005.
39. Field enhancement numbers quoted refer to the average field intensity at the tip ends of the rod particle. The field is averaged over a volume extending 10 nm off the end face, described in detail in the Supporting Information.
40. Verslegers, L.; Yu, Z.; Ruan, Z.; Catrysse, P.; Fan, S. From Electromagnetically Induced Transparency to Superscattering with a Single Structure: A Coupled-Mode Theory for Doubly Resonant Structures. *Phys. Rev. Lett.* **2012**, *108*, 1–5.
41. The ratio of the splitting energy to the line widths of the PA's plasmonic resonance and the PMMA vibrational mode are 0.27 and 2.24, respectively. For ref 37, the ratios of the splitting energy to the dipolar plasmonic mode's line width and the *J*-aggregate band's line width are roughly (based on inspection of Figure 2a–c in the reference) 0.48 and 3.5, respectively.